
© PHOTODISC & DIGITAL STOCK

An Autonomous Palm-Sized Gliding Micro Air Vehicle

Design, Fabrication, and Results of a Fully Integrated Centimeter-Scale MAV

The rapid design and prototyping of a passive micro air vehicle (MAV) with the final goal of locating and flying toward a target while avoiding hazardous obstacles is presented. This design incorporates a number of recently developed microrobotic materials and processes which serve as enabling technologies for such a platform. Articulated and rigid composite microstructures, high performance microactuators, low power biomimetic sensors, and efficient mechatronic and control systems are all adapted for use on a 10 cm, 2 g MAV capable of autonomous flight, target sensing, and obstacle avoidance.

Currently, there is a great deal of interest in the various categories of MAVs. Such devices can be loosely constrained to approximately 15 cm, and generally less than 100 g. There are many applications appropriate for MAVs including reconnaissance, hazardous environment exploration, and search and rescue. These applications may require various morphologies and thus MAVs can be broken into a number of classes such as fixed wing [1]–[6] flapping wing [7]–[14], or rotary wing [15]. One area which has remained somewhat sparse is passive MAVs [16]. This article explores the design, fabrication, and results for a palm-sized autonomous glider and describes subsystems which are relevant to all MAV classes. Figure 1 shows the most recent version of the MicroGlider.

A primary concern in designing this MAV is the power and mass budget allotted to each component. Preliminary estimates and measurements for each subsystem are shown in Table 1.

Airfoil, Fuselage and Control Surfaces

MAVs are attractive because of their small size and high maneuverability. However, these traits also raise important design considerations. To maximize the flight time for a given power source it is critical to optimize the lift producing surfaces. Similarly, in order to obtain the maximum maneuverability it is necessary to create suitable control surfaces. This section describes the aerodynamic basis for the physical structure of the MicroGlider.

Airfoil

As pointed out by Mueller and DeLaurier [17], lessons learned from airfoil design at high Reynolds numbers (above 2×10^5) are generally not applicable to low Reynolds number cases. Thus, to determine the optimal MicroGlider airfoil design, an empirical approach is used. To understand the effect of various geometric parameters on the airfoil efficiency (lift to drag ratio) a parameterization is chosen based upon computational fluid dynamic (CFD) modeling. Key parameters of the airfoil include aspect ratio (AR), chord length (l_c), camber percentage, and position of maximum camber. From the CFD analysis, a sample of these parameters is chosen and the appropriate airfoils are created using a composite molding process [18]. Each chosen airfoil is attached to a custom two axis force sensor capable of measuring normal and tangential forces with a resolution of approximately 10 μN. This transducer is fitted to a wind tunnel via a servo capable of subdegree resolution rotations. An anemometer measures the air

BY ROBERT J. WOOD, S. AVADHANULA, E. STELTZ, M. SEEMAN, J. ENTWISTLE,
A. BACHRACH, G. BARROWS, S. SANDERS, AND RONALD S. FEARING

1070-9932/07/$25.00©2007 IEEE

velocity such that the precise wind speed may be regulated by a traditional feedback control system. This velocity and the servo angle are controlled via xPC (from MathWorks, Natick, MA) as is shown in Figure 2.

The lift and drag coefficients are then measured as a function of both fluid velocity and angle of attack. Sample results are shown in Figure 3. From this optimization, airfoils with a lift-to-drag coefficient greater than 8 are achievable in this low Reynolds number environment (Re ≈ 7000).

Control Surfaces

For construction simplicity and minimal mass, a V-tail configuration is developed. The MicroGlider uses only two control surfaces, both mounted on the tail, which produce normal forces on the tail surfaces that map the two actuator inputs to roll, pitch, and yaw body torques. Similar to a microelectromechanical systems (MEMS) approach to create Micro-Flaps [19] using actuated hinged structures, the MicroGlider control surfaces are manipulated by piezoelectric bending actuators [20] which require a motion-amplifying transmission system that will be discussed in this section.

Control Surface Kinematics

The tail, actuator, and control surface form a closed parallel chain via an additional laser-micromachined link. The distal end of the actuator is connected to the control surface hinge through a slider-crank to form a four bar mechanism (similar to the mechanisms in [18] and [21]) as is shown in Figure 4. Thus, the small displacement (δ) of the actuator is amplified into a larger rotation (ϕ) at the base of the control surface.

The forward kinematics for such a chain are determined by the relative lengths of the constituent members [16]. Thus the amplification of the actuator motion can be selected based upon the relative geometries to ensure adequate body torques. To determine what deflection is sufficient to achieve the desired level of maneuverability, control surface forces are measured and transformed into torques using a simplified rigid body model of the MicroGlider.

Glider Torque Estimation

Due to power, mass, and size limitations, the processing power of the MicroGlider controller will be significantly less than that of traditional robotic systems. This places limits on the fidelity of control. One solution to this problem is to characterize the body torques produced by various control inputs and choose appropriate spaces in this map to generate independent body torques in a discrete manner. The first step in this process is to model the overall system by way of the following mapping:

$$\begin{bmatrix} s_l \\ s_r \end{bmatrix} \xrightarrow{T} \begin{bmatrix} \tau_r \\ \tau_p \\ \tau_y \end{bmatrix} \tag{1}$$

Table 1. Preliminary mass and power budgets.

Subsystem	**Mass (mg)**	**Power (mW)**
Airfoil	265	—
Fuselage	130	—
Control surfaces & tail	150	—
Actuators	50	3.5
Control/power PCB	440	—
H.V. electronics	—	6.5
control electronics	—	6
Optic flow	325	29
Sensors[1]	200	5
Battery	700	—
Total	2220	50

[1] goal specifications

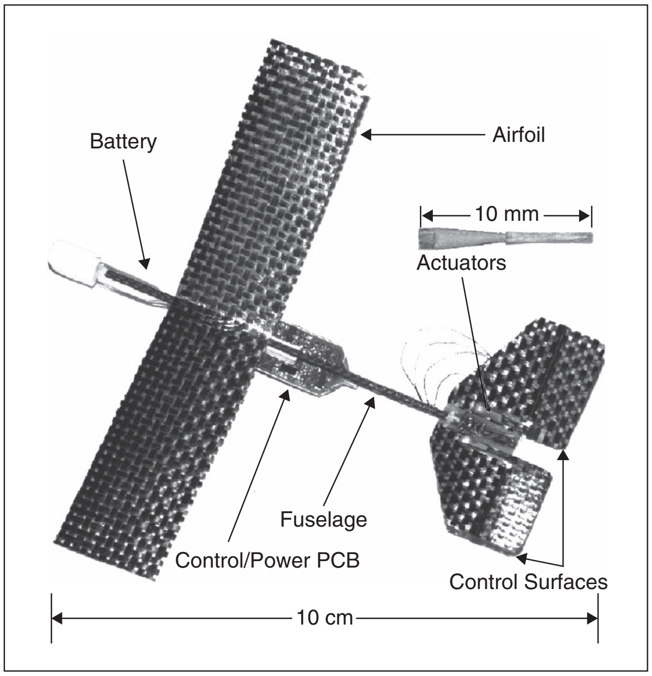

Figure 1. *Complete 2 g MicroGlider.*

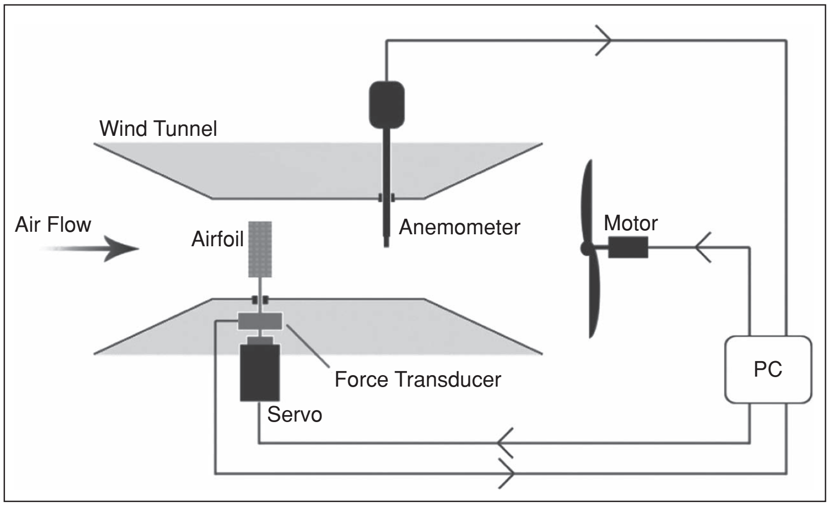

Figure 2. *Wind tunnel airfoil measurement setup.*

where the subscripts r, p, and γ represent roll, pitch, and yaw with respect to the body moments about the center of gravity (CG) and s_l and s_r are the left and right control signals. Ideally, this map would be measured directly as a two input, three output system using a three axis torque sensor while spanning the appropriate space of the two input voltages. This is impractical since existing multi axis torque sensors are either too insensitive ($>>$ 10mN-mm resolution), have insufficient bandwidth ($<$ 100Hz), or are simply too bulky to be placed in the wind tunnel with the glider. As an alternate approach, the individual control surface lift and drag forces are measured using the airfoil setup shown in Figure 2. A single control surface is rigidly attached to the two-axis force sensor and the lift and drag are measured as a function of the actuator input voltage. Now the following mapping can be described:

$$[s] \xrightarrow{T_s} \begin{bmatrix} F_{\text{lift}} \\ F_{\text{drag}} \end{bmatrix} \tag{2}$$

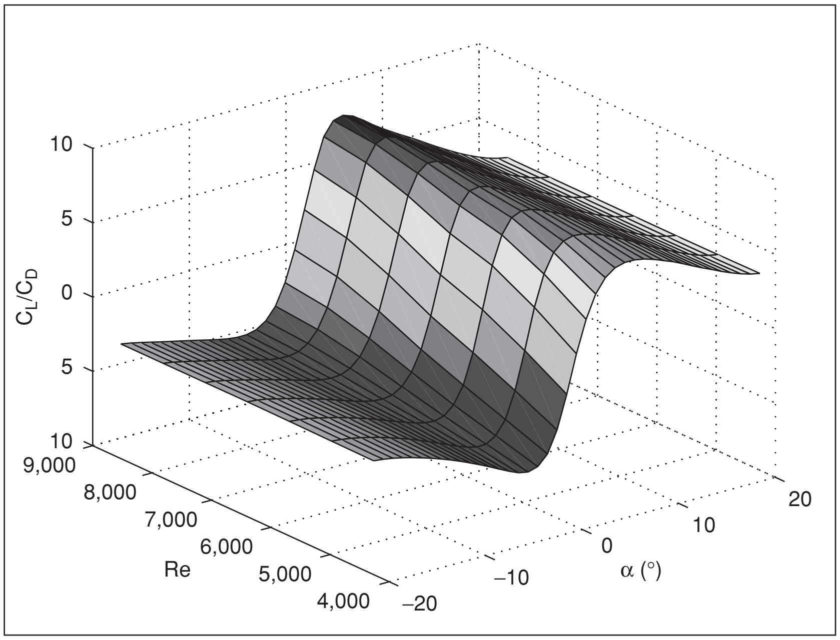

Figure 3. *Lift and drag coefficients for a sample airfoil.*

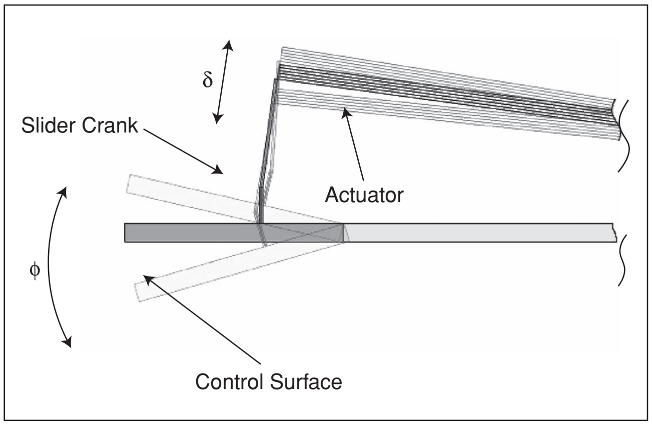

Figure 4. *Detail of control surface transmission system.*

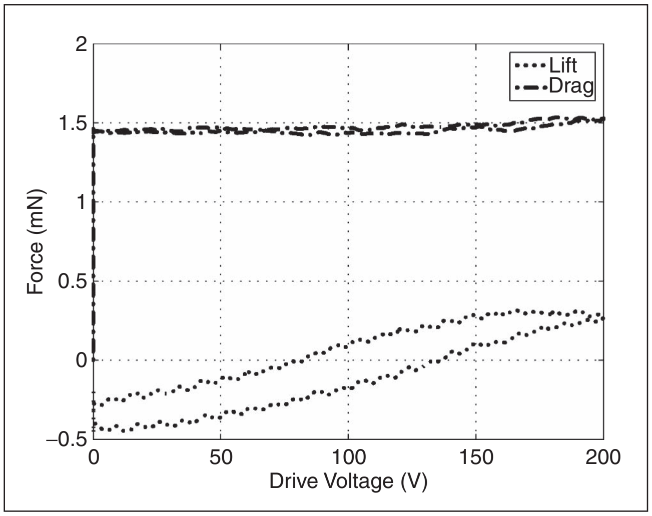

Figure 5. *Control surface lift (normal) and drag (tangential) measurements as a function of actuator voltage. Note that the drag is relatively independent of the applied voltage.*

This map can be used to develop the desired mapping (1) through the glider geometry. An example of this map is shown in Figure 5.

Now let θ, l_e, and l_f represent the 'V-tail' dihedral angle, the distance from the fuselage to the individual control surface center of pressure, and the length from the CG to the control surface center of pressure respectively (see Figure 6). Thus, a simplified map from control surface lift forces to body torques can be derived and is shown in the following:

$$\begin{bmatrix} \tau_r \\ \tau_p \\ \tau_\gamma \end{bmatrix} = \begin{bmatrix} l_e & -l_e \\ l_f \sin(\theta/2) & l_f \sin(\theta/2) \\ l_f \cos(\theta/2) & -l_f \cos(\theta/2) \end{bmatrix} \begin{bmatrix} F_l \\ F_r \end{bmatrix} \tag{3}$$

where F_l and F_r are the control surface normal forces from (2) for the left and right control surface respectively (again, see Figure 6). Note again that since the control surface drag forces are constant, they are a static disturbance and will not be considered in the formulation of the body torques. Finally, these two maps are combined (along with linearized control surface lift data from Figure 5) to give the desired map T. Subsections of this map are used by the flight control system to perform appropriate maneuvers during flight. The expected magnitudes range from ±20mN-mm roll, ±50mN-mm pitch, and ±50mN-mm yaw.

Fuselage and Fabrication

The airfoil, control surfaces, tail, and fuselage each consist of ultra high modulus composite materials. This gives great versatility to the manufacturing process since unidirectional or woven lamina of these materials are easily molded. In addition, the composites are initially in a form called prepreg which consists of sheets of bundled fibers impregnated with a catalyzed but uncured epoxy. The epoxy in these lamina negates the need for additional bonding layers when forming more complex structures. The airfoil is cut as a prepreg and compression molded while curing to give the desired cross section (as determined previously). The control surfaces are also cut as prepreg and are fixed in a mold with the cylindrical carbon fiber fuselage and cured. The control surfaces are fixed to the tail via laser-micromachined links and hinges to form the transmission [18]. Finally, the actuators are fixed to the tail and wired by hand.

There are many applications appropriate for MAVs including reconnaissance, hazardous environment exploration, and search and rescue.

Control and Power Electronics

As seen in Figure 1, the electronics and control reside on a discrete PCB mounted to the center portion of the fuselage. This board performs all control tasks, collaborates sensing and communication, conditions the battery power, protects the battery with low voltage detection, and contains the high voltage electronics required to control the actuators. Figure 7 displays an overview of the electronics on board the MicroGlider. The power for the MicroGlider is supplied by a single 20 mAh lithium polymer (LiPo) battery. This chemistry allows very high discharge rates (>5C) and can thus yield approximately 400 mW for 10 min flight durations.

Several commercially available control boards were considered, including products by Softbaugh (part number T1121, 1.7 g) and Didel (for example, WdPicDev84). However, the MicroGlider requires a board under 500 mg (including high voltage electronics). Since the MicroGlider will employ piezoelectric actuators, some type of power amplifier to boost the battery voltage to 200 volts is required. To the authors' knowledge, no existing board meets these specifications.

Other researchers have constructed custom piezoelectric microrobot control boards, such as Brufau, et al. [22] and Montane, et al. [23]. However, most of these boards are meant to power piezoelectric stack actuators, which require voltages much lower than the MicroGlider's cantilever actuators (≈ 20–50 V for stack actuators versus 200 V for the bimorphs used here).

Power Electronics

The bimorph piezoelectric actuators require both a high-voltage bias supply (V_b) and a drive signal (V_d) ranging between ground and V_b to create displacement (see [20] for details on this drive method). To minimize weight, a pulse-width modulated n-channel MOSFET in series with a pair of resistors is used to modulate the bias supply. A 10-MΩ resistor is used to charge the actuator and a 2-MΩ resistor is used to discharge the actuator. The time constant associated with the actuator's capacitance and these series resistors filters the PWM square wave to create the desired low-frequency waveform. The amplifier and bimorph schematics are shown in Figure 8.

Piezo Bias dc-dc Converter

There are a number of existing approaches to boost the battery voltage to the desired bias level, however low mass and

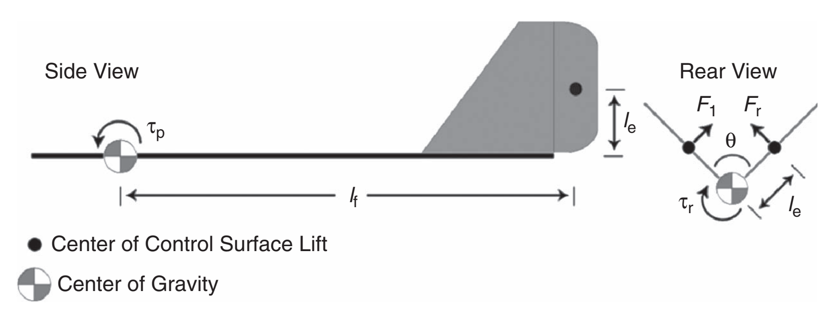

Figure 6. *Simplified glider drawing showing rigid body geometric parameters.*

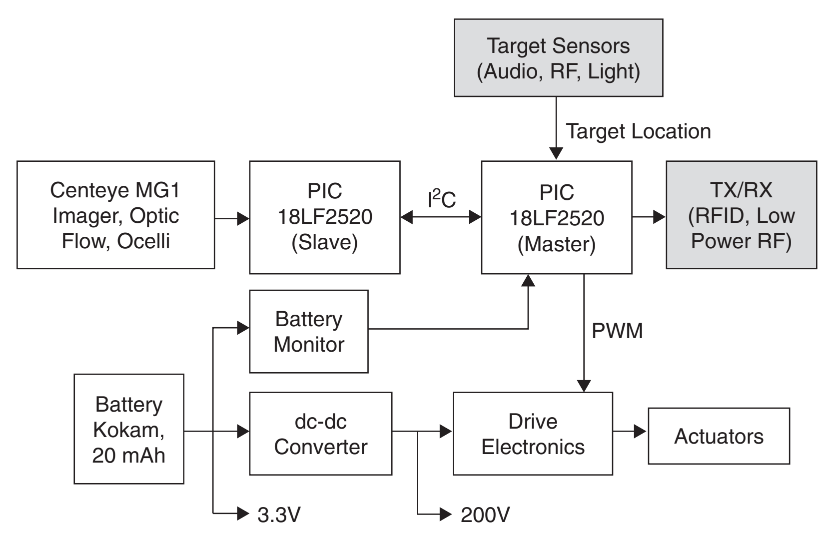

Figure 7. *Block diagram of glider electronics and control. Filled boxes represent work in progress.*

high efficiency are crucial in this application. A custom IC is desirable but is cost prohibitive and has an extensive lead time. Instead, a low-power boost converter (Linear Technology LTC1615-1) is used as a first boost stage. This topology (Figure 9) uses a simple inductor rather than a heavier transformer. A pulsed waveform (ranging between zero and 32 V) is formed across the boost converter diode. The charge-pump multiplies this voltage by a factor of *n* (ideally), where *n* is the number of charge pump stages, to produce the bias voltage.

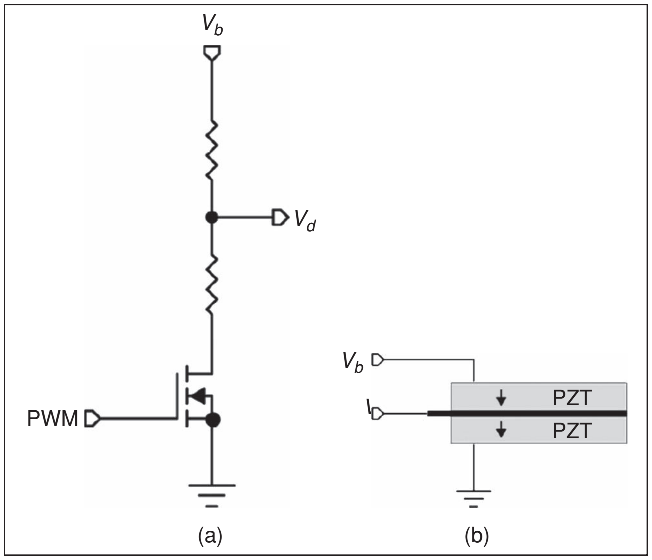

Figure 8. *(a) Schematics of amplifier. (b) Dual-source bimorph drive method.*

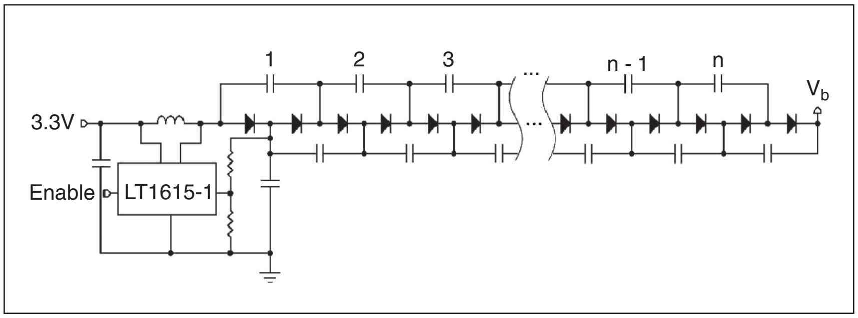

Figure 9. *Schematic of boost converter and chargepump stages used to create the high voltage supply.*

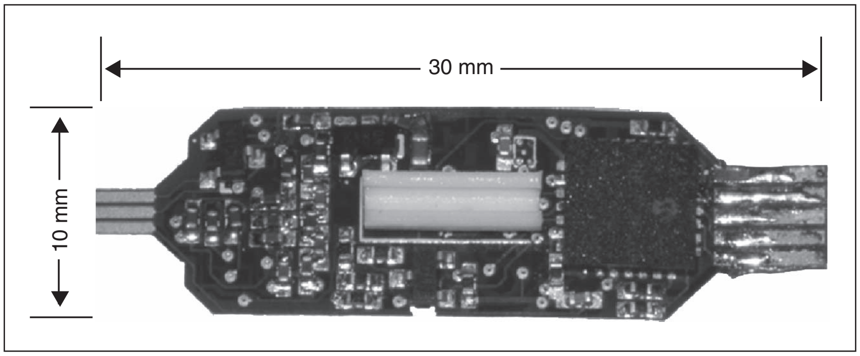

Figure 10. *MicroGlider power/control board (top side).*

Although the charge pump involves a number of capacitors and diodes, its weight is minimized through the use of 0402 capacitors and multidiode surface-mount components. When built, the converter outputs 205 V when driven from the battery (using seven charge pump stages). Over the expected operating range, the converter is between 51 and 63 percent efficient. The losses are attributed to the quiescent power draw and switching loss of the boost converter IC. The dc output impedance is 48.2 kΩ and the bandwidth is 3 Hz. The converter's components weigh approximately 120 mg, neglecting the PCB weight, and occupy 70 mm^2 of board space (with components on both sides).

Control Electronics

The MicroGlider master processor is the Microchip PIC 18LF2520. This processor was chosen for its internal oscillator, low power consumption, and small outline (28 pin QFN package, approximately 90 mg). The microcontroller also has two PWM outputs (to switch the two drive MOSFETs) and several A/D converters to measure sensors on the board. Additionally, the microcontroller interface to the optical flow sensor is straightforward using the I2C protocol (as discussed in the following). The completed board (shown in Figure 10) weighs 440 mg, and consumes approximately 12.5 mW (driving actuators and running a program at 1 MIPS).

Figure 11 shows a simulation for both the drive voltage, V_d, and output power for a 250 Hz PWM signal controlling one actuator. Note that since the load is mostly capacitive, the power required to hold an actuator at a given field is very low. Also, note that in Figure 11 the drive voltage is a nonlinear function of the duty cycle. Since this is a known nonlinearity it can be compensated for. This nonlinearity arises from the simplicity of the drive method and could easily be corrected with the consequence of lower efficiency and higher mass.

Sensors and Navigation

The MicroGlider is fitted with an optical flow sensor for obstacle avoidance and with a target localizing sensor. This architecture is biomimetic in nature and as such, biomimetic sensor morphologies and control strategies will be presented and discussed in this section.

Target Localization

A typical mission for the MicroGlider involves locating a target and descending toward it while avoiding obstacles. Two target localization sensors are proposed here, however, the general control architecture is identical for any of these. Minimal power and mass are emphasized in the selection and design of sensor technologies.

First, inspired by the optical horizon detection sensor found in many insects [24], a light source sensor called an ocelli is developed for global orientation estimation [25]. This sensor uses discrete photoreceptors (photodiodes or phototransistors) to view distinct areas of the sky sphere. Pair-wise subtraction of bilateral ocellus signals gives an estimate of the body orientation with respect to a prominent light source. Figure 12 shows the output of a prototype ocelli when its orientation relative to a fixed light source is varied.

Second, tracking an audio source is possible via two microphones positioned at distant geometric locations on the glider. The sound signals detected by the two microphones are fed into two hardware phase locked loops (PLLs) [16]. The voltage controlled oscillator output of each PLL is a pulse train phase locked to the input sound signal. This works well since the signal to be detected is expected to be narrow-band. The two pulse trains are then fed into a hardware XOR gate. By measuring the duration for which the XOR gate is high, the duration for which the two pulse trains have differing values can be calculated. Since the pulse trains are phase locked to the incoming sound signals, the duty cycle of the XOR output is directly proportional to the phase difference of the two incoming sound signals. This phase difference is proportional to the direction of the target. The audio sensor was prototyped and proved the concept by accurately detecting the source location up to a distance of approximately 20 m.

To determine the optimal MicroGlider airfoil design, an empirical approach is used.

Saccade-Based Navigation

The higher level navigation scheme is split into two distinct phases: far field navigation and near field navigation, based on whether the MicroGlider is far from or near the target respectively.

In far field navigation, the controller attempts to fly the MicroGlider directly toward the target using one of the sensors described in the previous section. When the MicroGlider

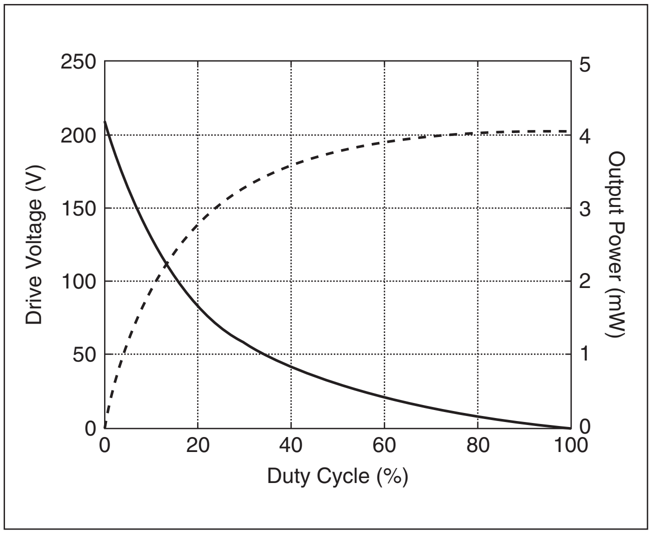

Figure 11. *Drive voltage V_d (solid) and power (dashed) as a function of PWM duty cycle.*

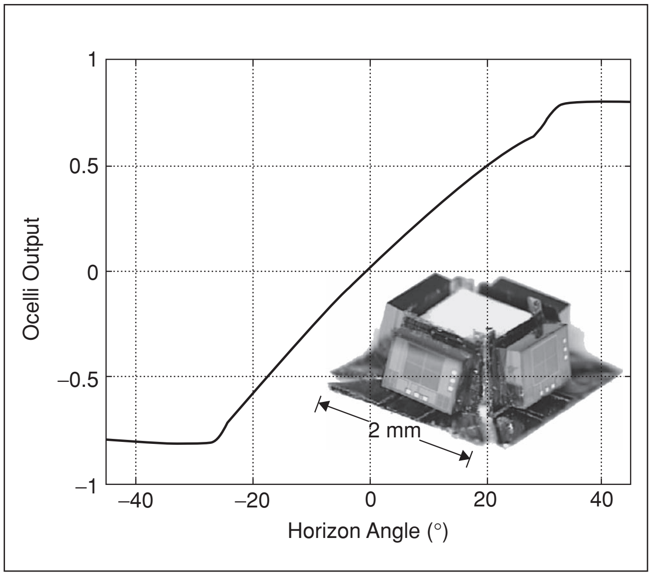

Figure 12. *Ocelli response to rotation in the presence of a fixed light source.*

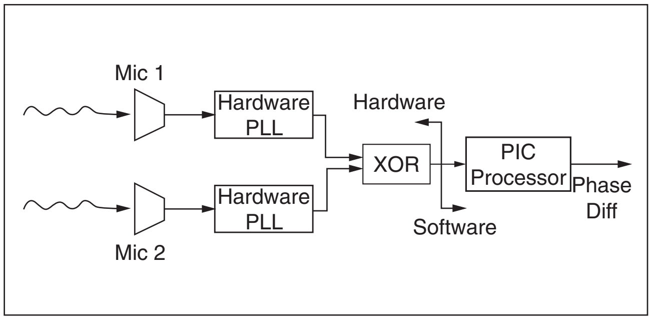

Figure 13. *Audio target localization overview.*

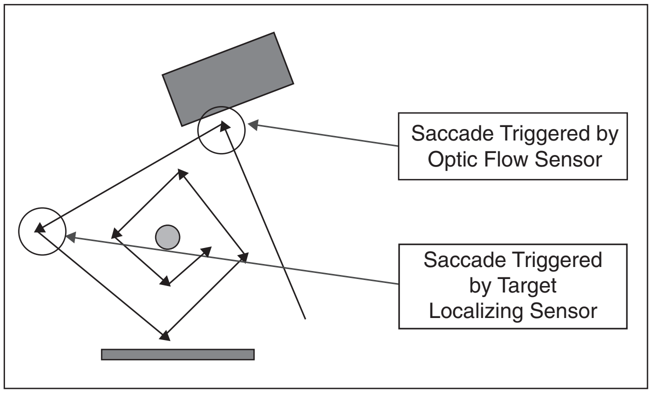

Figure 14. *Near field navigation scheme.*

Tracking an audio source is possible via two microphones positioned at distant geometric locations on the glider.

detects that it is sufficiently close to the target, the controller switches to a saccade-based homing algorithm inspired by the navigation of real insects [26]. In this scheme (shown in Figure 14), the MicroGlider tries to keep the target directly to the right (or left). In this manner, the aircraft flies without any navigation input (i.e., in straight line segments) until either the optical flow sensor detects an obstacle or the target is no longer on its right (or left).

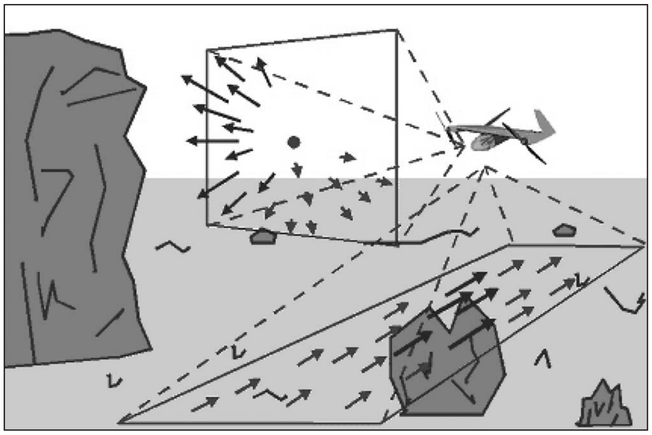

Figure 15. *Optical flow, as seen from an aircraft.*

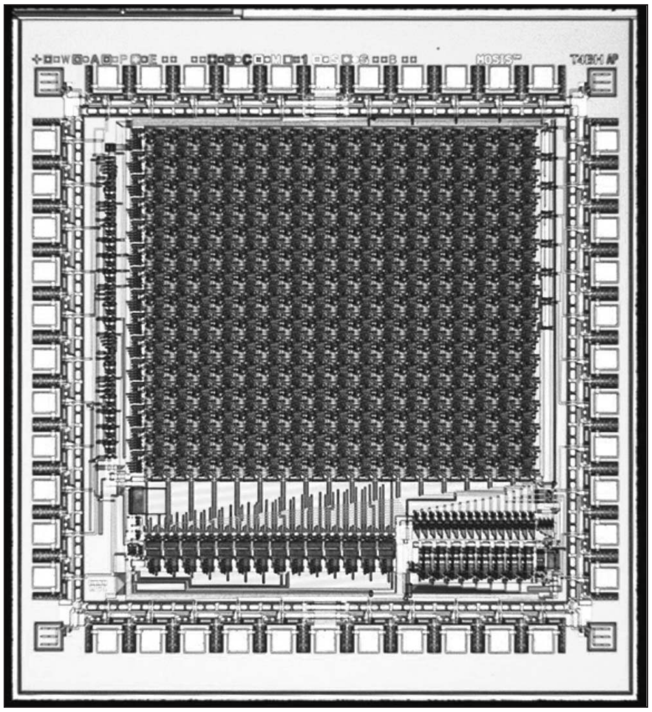

Figure 16. *Photograph of optical flow vision chip.*

Optical Flow Architecture and Implementation

Obstacles will be detected and avoided with the use of optical flow sensing. Optical flow [27] is the apparent visual motion that results from relative motion between an imager (or eyeball) and other objects in the environment (Figure 15). Consider an aircraft traveling in the forward direction. The ground will appear to move from front to back, with a rate that increases as the aircraft approaches the ground or as the glider flies over tall objects. Objects in front of the aircraft will grow in size, creating an expanding optical flow pattern. If the aircraft approaches a wall or tree line at an angle, the optical flow in the direction of that object will increase, indicating an imminent collision.

In order to integrate the imaging and image processing in a package suitable for integration onto the MicroGlider, a custom vision chip for optical flow processing has been designed. A die photograph of the vision chip is shown in Figure 16. This vision chip includes both image acquisition and low-level image processing on the same die. The architecture and circuitry is similar to that used in optical flow sensors developed by Barrows in earlier work [28]. The vision chip forms the focal plane of a camera-like imaging system. The image itself is formed by a lens or a pinhole. A 15-by-17 array of photoreceptors grabs a low-resolution image of the environment. An array of feature detectors, implemented with simple analog circuits, computes the presence of edges, saddle points, or other features in the visual field. The last layer of processing on the vision chip analyzes the feature detector outputs, and generates a single bit for each pixel. The bit is high or low indicating the presence or absence of a particular feature of interest. The optical flow processing is completed with a PIC 18LF2520, identical to the master MicroGlider microcontroller. Optical flow is computed by tracking the motion of the high bit values generated by the vision chip. The optical flow sensor communicates with the power/control board using the I2C serial interface built into these microcontrollers.

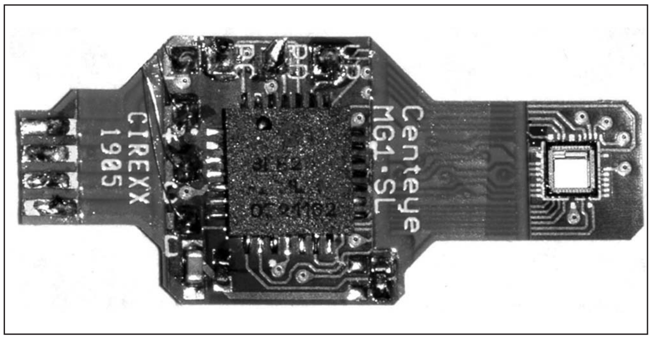

Figure 17. *325 mg optical flow sensor prototype. The optics over the vision chip have been removed for display purposes.*

Earlier versions of these optical flow sensors have been fabricated in packages weighing 4.5 g, which is clearly too heavy for the MicroGlider. However by using QFN-packaged PICs, extremely thin PC board material, and bare vision chip dies, we have been able to reduce the mass of a single optical flow sensor to 325 mg (with a pinhole lens). Figure 17 shows one prototype sensor, fabricated on the same flex-circuit material as the power/control board shown in Figure 10.

Obstacle avoidance will be performed using various flight-control strategies observed in flying insects. The reader is referred to another paper [29] for a compilation of flight control strategies. Sample strategies include turning away from regions of high optical flow to avoid obstacles, equalizing optical flow on the left and right sides to fly down a corridor, and making zig-zag flight patterns to detect narrow objects.

Simulation

To assist in design and testing, a software tool has been developed to accurately simulate the MicroGlider in flight. This simulator is being used to quickly evaluate body design changes to the MicroGlider and their effects in a virtual environment. In addition, the use of the simulator to test the performance of different flight control algorithms has begun.

The simulator is a three-axis, six-degree-of-freedom simulator implemented in Matlab. The simulator combines classic rigid body dynamics with empirically measured MicroGlider parameters to calculate the state of the system during a virtual flight. The model parameters used in the simulator include the mass and inertial matrix of the MicroGlider, the size and position of various glider components, as well as the lift and drag coefficients of the wings, body, and tail. These parame-

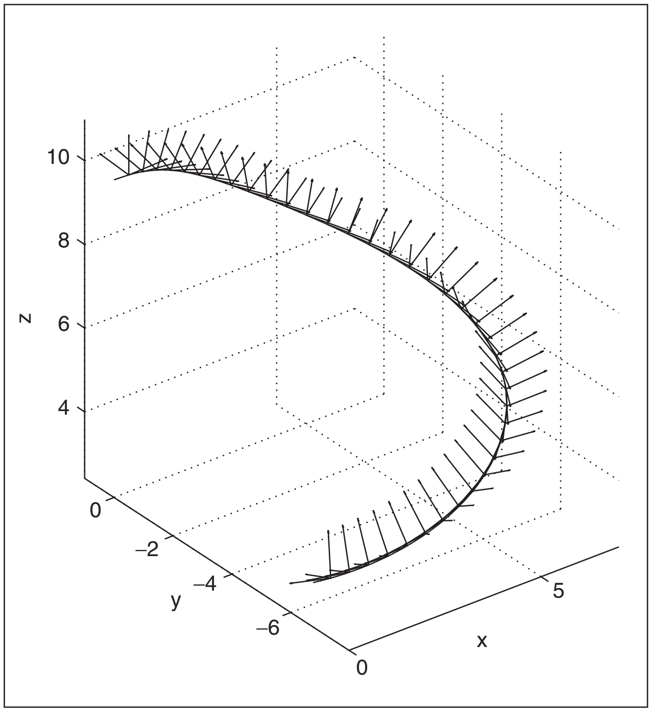

Figure 18. *Simulated MicroGlider executing a steady turn to the right after initial horizontal launch (arrows represent the local coordinate frame for each time step).*

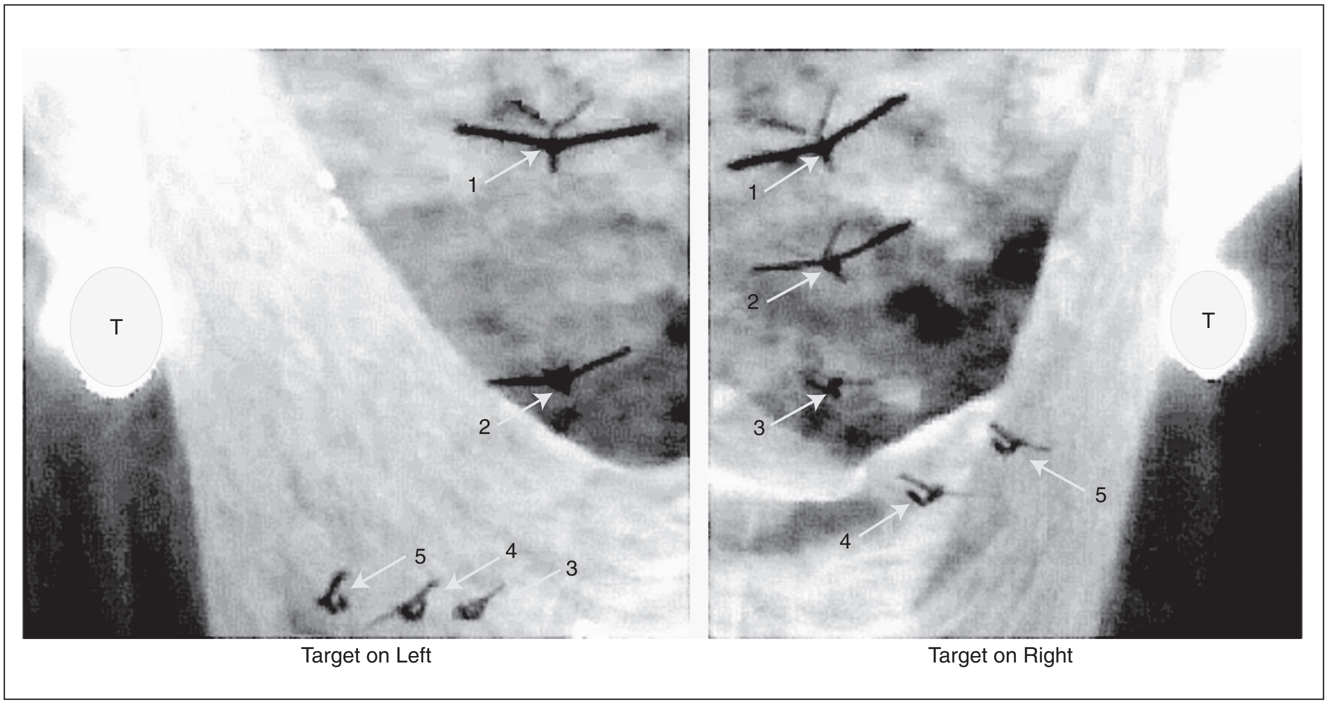

Figure 19. *Left and right turns toward a light source. This image is the combination of a sequence of five video frames (the initial flight direction is into the page and the sequence is labeled in ascending time order) where the gliders are indicated by the arrows and the light sources are the bright areas (marked with a "T") on the left and right, respectively.*

The low costs of most components allow rigorous testing to be done without worry of substantial damage.

ters can be modified to analyze their effects and maximize flight performance.

In addition to simulating the trajectory of the MicroGlider, the simulator is used to estimate the response for the various sensor configurations discussed in previous sections, as well as different simulated environments. This allows the user to evaluate what the MicroGlider perceives, and to utilize this information to design superior control strategies. As an example of the simulator functionality, Figure 18 shows the predicted response for a typical flight mode.

Discussion

This article has concentrated on the development of a set of core technologies key to the realization of an autonomous 2-g glider. One aspect which was not discussed in detail was the ease of construction and low cost of an individual MicroGlider. Integration is simplified through a number of rapid prototyping techniques and the low costs of most components allow rigorous testing to be done without worry of substantial damage.

Integration

The five subsystems, control surfaces and fuselage, airfoil, control PCB, imager PCB, and battery are integrated together using molded short-fiber composite clips. This allows each piece to remain modular and its position with respect to the CG to be adjustable. Once each subsystem is completed, the glider is attached to a low friction model aircraft balance and the position of each piece is selected to place the CG in the desired position (with respect to the roll and pitch axes). The effect of altering the CG can be observed with the flight simulator, however it is generally understood that it should be slightly forward and slightly below the center of lift for maximum stability and maneuverability.

Initial Flight Tests

Two initial tests are described here which demonstrate the functionality of the MicroGlider: A turning test without a stimulus and a test with bilaterally positioned light sources to trigger a turn. Both tests were performed in a controlled laboratory environment using a custom launch apparatus to ensure consistency in the initial flight conditions. The purpose of the first turning test (the open-loop test) is to calibrate the MicroGlider response to control surface actuation. Once the turns were effectively tuned by adjusting the magnitude and timing of the control surface actuation, the MicroGlider was fitted with an ocelli and a light source was positioned on either side. The controller was programmed to trigger a saccade toward the light source when it was detected on either side. Sample flight sequences are shown in Figure 19.

Note that Figure 19 shows the MicroGlider initiating a turn shortly after release in the direction of the target light source. This test demonstrated that the MicroGlider was able to recognize a target stimulus in flight and react appropriately.

Acknowledgments

This material is based upon work supported by the National Science Foundation (NSF) under Grant IIS-0412541. Any opinions, findings, conclusions, or recommendations expressed in this material are those of the author(s) and do not necessarily reflect the views of the NSF. The authors would like to gratefully acknowledge the Defense Advanced Research Projects Agency for support under Fund\#FA8650-05-C-7138.

Keywords

Micro air vehicles, aerial robotics, optical flow, target tracking.

References

[1] W. Green and P. Oh, "An aerial prototype for situational awareness in closed quarters," in *Proc. IEEE/RSJ Int. Conf. Intelligent Robots Systems*, Las Vegas, NV, Oct. 2003, pp. 61–66.

[2] T. Mueller and J. DeLaurier, "Aerodynamics of small vehicles," *Annu. Rev. Fluid Mech.*, vol. 35, pp. 89–111, 2003.

[3] J.-D. Nicoud and J.-C. Zufferey, "Towards indoor flying robots," in *Proc. IEEE/RSJ Int. Conf. on Intelligent Robots and Systems*, Lausanne, Switzerland, Oct. 2002, pp. 787–792.

[4] S. Sunada, T. Yasuda, K. Yasuda, and K. Kawachi, "Comparison of wing characteristics at an ultralow reynolds number," *J. Aircraft*, vol. 39, no. 2, pp. 331–338, 2002.

[5] H.-Y. Wu, D. Sun, Z.-Y. Zhou, S.-S. Xiong, and X.-H. Wang, "Micro air vehicle: Architecture and implementation," in *Proc. IEEE Int. Conf. Robotics Automation*, Taipei, Taiwan, Sept. 2003, pp. 534–539.

[6] M. Keennon and J. Grasmeyer, "Development of the Black Widow and Microbat MAVs and a vision of the future of MAV design," in *Proc. AIAA/ICAS Intl. Air and Space Symp. and Exposition: The Next 100 Years*, Dayton, OH, July 2003, AIAA-2003–2901.

[7] S. Avadhanula, R. Wood, D. Campolo, and R. Fearing, "Dynamically tuned design of the MFI thorax," in *Proc. IEEE Int. Conf. on Robotics and Automation*, Washington, DC, May 2002, pp. 52–59.

[8] S. Banala, Y. Karakaya, S. McIntosh, Z. Khan, and S. Agrawal, "Design and optimization of a mechanism for out of plane insect wing motion with twist," in *Proc. of DETC, ASME Design Engineering Technical Conferences*, Salt Lake City, UT, Sept. 2004.

[9] R. Madangopal, Z. Khan, and S. Agrawal, "Biologically inspired design of small flapping wing air vehicles using four-bar mechanisms and quasi-steady aerodynamics," *J. Mech. Design*, vol. 127, pp. 809–816, July 2005.

[10] A. Cox, D. Monopoli, M. Goldfarb, and E. Garcia, "The development of pizeoelectrically actuated micro-air vehicles," in *Proc. SPIE Conf. on Microrobotics Microassembly*, Boston, MA, Sept. 1999, vol. 3834, pp. 101–108.

[11] A. Cox, D. Monopoli, D. Cveticanin, M. Goldfarb, and E. Garcia, "The development of elastodynamic components for piezo-electrically actuated flapping micro-air vehicles," *J. Intell. Mater. Syst. Struct.*, vol. 13, pp. 611–615, Sept. 2002.

[12] T.N. Pornsin, S.W. Lee, H. Nassef, J. Grasmeyer, Y.C. Tai, C.M. Ho, and M. Keennon, "Mems wing technology for a battery powered

ornithopter," in *Proc. 13th IEEE Anual Int. Conf. MEMS,* Miyazaki, Japan, Jan. 2000, pp. 709–804.
[13] T.N. Pornsin-shiriak, Y.C. Tai, H. Nassef, and C.M. Ho, "Titanium-alloy MEMS wing technology for a micro aerial vehicle application," *J. Sensors Actuators A: Phys.*, vol. 89, pp. 95–103, Mar. 2001.
[14] J. Yan, R. Wood, S. Avadhanula, and M.S. amd R.S. Fearing, "Towards flapping wing control for a micromechanical flying insect," in *Proc. IEEE Int. Conf. Robotics and Automation*, Seoul, Korea, May 2001, pp. 3901–3908.
[15] I. Kroo and P. Kunz, "Meso-scale flight and miniature rotorcraft development," in *Fixed and Flapping Wing Aerodynamics for Micro Air Vehicle Applications* (Progress in Astronuatics and Aeronautics, American Institute of Aeronautics and Astronautics Series), vol. 195. Reston, VA: AIAA: 2001.
[16] R. Wood, S. Avadhanula, E. Steltz, M. Seeman, J. Entwistle, A. Bachrach, G. Barrows, S. Sanders, and R. Fearing, "Design, fabrication and initial results of a 2 g autonomous glider," in *Proc. Conf. IEEE Industrial Electronics Society*, Raleigh, NC, Nov. 2005.
[17] T. Mueller and J. DeLaurier, "An overview of micro air vehicle aerodynamics," in *Fixed and Flapping Wing Aerodynamics for Micro Air Vehicle Applications* (Progress in Astronuatics and Aeronautics, American Institute of Aeronautics and Astronautics Series), vol. 195. Reston, VA: AIAA: 2001.
[18] R. Wood, S. Avadhanula, M. Menon, and R. Fearing, "Micro-robotics using composite materials: The micromechanical flying insect thorax," in *Proc. IEEE Int. Conf. Robotics Automation*, Taipei, Taiwan, Sept. 2003, pp. 1842–1849.
[19] Y.-C. Tai, "Aerodynamic control of a delta-wing using MEMS sensors and actuators," in *Proc. Int. Symp. Micromechatronics Human Science*, Nagoya, Japan, pp. 21–26, 1997.
[20] R. Wood, E. Steltz, and R. Fearing, "Optimal energy density piezoelectric bending actuators," *J. Sensors Actuators A: Phys.*, vol. 119, no. 2, pp. 476–488, 2005.
[21] A. Cox, E. Garcia, and M. Goldfarb, "Actuator development for a flapping microrobotic microaerial vehicle," in *Proc. SPIE Conf. Microrobotics Micromanipulation*, Boston, MA, Nov. 1998, vol. 3519, pp. 102–108.
[22] J. Brufau, M. Puig-Vidal, J. López-Sánchez, J. Samitier, W. Driesen, J. Breguet, N. Snis, U. Simu, S. Johansson, and T. Velten, "MICRON: Small autonomous robot for cell manipulation applications," in *Proc. IEEE Int. Conf. Robotics Automation*, Barcelona, Spain, Apr. 2005, pp. 844–849.
[23] E. Montane, P. Miribel-Catala, J. Lopez-Sanchez, M. PuigVidal, S. Bota, and J. Samitier, "High-voltage smart power integrated circuits to drive piezoceramicactuators for microrobotic applications," *IEEE Proc. Circuits, Devices, Systems*, vol. 148, no. 6, pp. 343–347, 2001.
[24] H. Schuppe and R. Hengstenberg, "Optical properties of the ocelli of Calliphora erythrocephala and their role in the dorsal light response," *J. Comparat. Physiol. A*, vol. 173, no. 2, pp. 143–149, 1993.
[25] W. Wu, L. Schenato, R. Wood, and R. Fearing, "Biomimetic sensor suite for flight control of a micromechanical flying insect: Design and experimental results," in *Proc. IEEE Int. Conf. on Robotics and Automation*, Taipei, Taiwan, Sept. 2003, pp. 1146–1151.
[26] M. Dickinson, L. Tammero, and M. Tarstino, "Sensory fusion in free-flight search behavior of fruit flies," in *Neurotechnology for Biomimetic Robots*. Cambridge, MA: MIT Pres, Sept. 2002s, pp. 573–591.
[27] J. Gibson, *The Ecological Approach to Visual Perception*. Boston, MA: Houghton Mifflin, 1950.
[28] G. Barrows, *Fixed and Flapping Wing Aerodynamics for Micro Air Vehicle Applications* (Progress in Astronautics and Aeronautics Series). Reston, VA: AIAA, 2001, vol. 195, ch. 26.
[29] G. Barrows, J. Chahl, and M. Srinivasan, "Biologically inspired visual sensing and flight control," *Aero. J. Royal Aero. Soc.*, vol. 107, no. 1069, pp. 159–168, Mar. 2003.

Robert J. Wood received a M.S. degree in 2001 and a Ph.D. in 2004, both in EECS from University of California at Berkeley. He is an assistant professor in the School of Engineering and Applied Sciences at Harvard University where he has been since January 2006. His research interests include the mechatronics of microrobotic devices, particularly mobile microrobots for aerial, terrestrial, and aquatic environments. He is also interested in the control of under-actuated processor-limited systems.

S. Avadhanula is with the Dept. of Electrical Engineering and Computer Sciences at University of California, Berkeley.

E. Steltz is with the Dept. of Electrical Engineering and Computer Sciences at University of California, Berkeley.

M. Seeman is with the Dept. of Electrical Engineering and Computer Sciences at University of California, Berkeley.

J. Entwistle is with the Dept. of Electrical Engineering and Computer Sciences at University of California, Berkeley.

A. Bachrach is with the Dept. of Electrical Engineering and Computer Sciences at University of California, Berkeley.

G. Barrows is with Centeye, Inc., Washington, DC.

S. Sanders is a professor in the Dept. of Electrical Engineering and Computer Sciences at University of California, Berkeley.

Ronald S. Fearing received S.B. and S.M. degrees in electrical engineering and computer sciences from MIT in 1983 and a Ph.D. in electrical engineering from Stanford in 1988. He is a professor in the Dept. of Electrical Engineering and Computer Sciences at University of California, Berkeley, which he joined in January 1988. He was Vice-Chair for Undergraduate Matters from 2000-2006. His current research interests are in microrobotics, including flying and crawling microrobots, microassembly, parallel nanograsping, and rapid prototyping. He has worked in tactile sensing, teletaction, and dextrous manipulation. He received the Presidential Young Investigator Award in 1991, and is the coinventor on five U.S. patents.

Address for Correspondence: Robert J. Wood, School of Engineering and Applied Sciences, Harvard University, Cambridge, MA 02138 USA. E-mail: rjwood@eecs.harvard.edu.